Shape of the two-photon-continuum emission from the $1s2s\,^1S_0$ state in He-like krypton

R. Ali,[*] I. Ahmad, R. W. Dunford, D. S. Gemmell, M. Jung, and E. P. Kanter
Physics Division, Argonne National Laboratory, Argonne, Illinois 60439

P. H. Mokler
GSI, D-64291 Darmstadt, Germany

H. G. Berry and A. E. Livingston
Department of Physics, University of Notre Dame, Notre Dame, Indiana 46556

S. Cheng and L. J. Curtis
Department of Physics and Astronomy, University of Toledo, Toledo, Ohio 43606
(Received 16 September 1996)

We report a measurement of the spectral distribution of photons from the two-photon decay of the $1s2s\,^1S_0$ level in heliumlike krypton. In the experiment, a beam of Kr^{34+} ions was excited using a thin carbon foil and the two-photon decays were observed as coincidences in an array of x-ray detectors. An important part of this work was the measurement of the efficiency of the detection system as a function of photon energy. A Monte Carlo model of the experiment was used to compare the data with theoretical calculations and demonstrated good agreement with the nonrelativistic calculations for $Z=36$. [S1050-2947(97)05502-9]

PACS number(s): 32.70.Fw, 31.30.Jv, 31.10.+z, 32.30.Rj

I. INTRODUCTION

The phenomenon of two-photon decay was first discussed by Maria Göppert-Mayer during the infancy of quantum mechanics more than 65 years ago [1,2]. In this process, also known as double-photon decay, a transition between quantum levels occurs via simultaneous emission of two photons. The calculation of the probability for such a transition requires summing over all bound and continuum states of the system. The individual photon energies from these decays form a continuum, but the sum of the energies of the two coincident photons is equal to the transition energy (within the natural width). In addition to the early pedagogic interest in quantum theory of two-photon decay, this decay mode was also of considerable importance in applications to astrophysics [3,4]. For example, it has been speculated that this process contributes to the continuum radiation from planetary nebulas [4]. The main interest at the present time is in comparisons between theoretical calculations and laboratory experiments in few-electron ions. In this connection, it is significant that two-photon decay tests our knowledge of the entire structure of the atom. This is because both energy levels and wave functions for a complete set of intermediate states must be known, a very rigorous challenge for theory.

In this paper, we describe a measurement of the spectral shape of the continuum radiation from the two-photon decay of the $1s2s\,^1S_0$ level in He-like krypton (see Fig. 1). This study complements our earlier work on the lifetime of this level in He-like Br [5], and the measurement by Marrus *et al.* [6] in He-like Kr. Measurements of the spectral shapes provide additional information on the details of the two-photon

transition probabilities, beyond the lifetime measurements which only test those probabilities summed over all continuum photon energies.

In Sec. II we briefly review the current status of experiment and theory for two-photon decay in atomic and nuclear physics. In Sec. III we describe the experimental apparatus for our measurement, and in Sec. IV we discuss the methods used to determine the efficiencies of the detectors as a function of photon energy which was a crucial requirement for the measurement. A Monte Carlo simulation of our experiment is described in Sec. V. This was used to aid in understanding the apparatus and to compare our results with theory. Finally, in Sec. VI we present our results and comment on the outlook for future work.
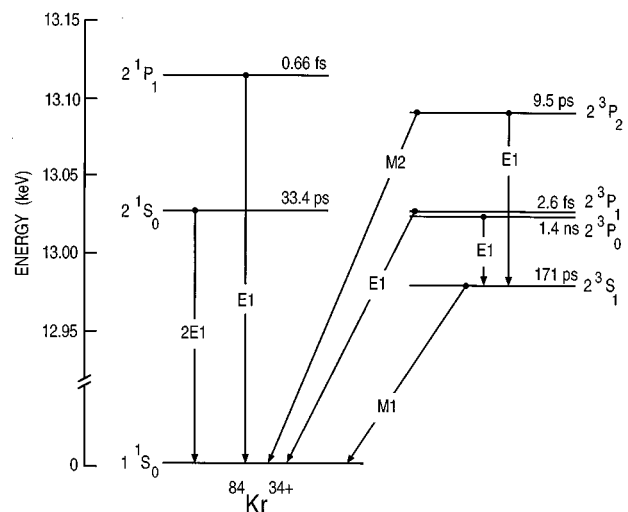

FIG. 1. Low-lying energy levels of He-like Kr showing lifetimes and decay modes.

---

*Present address: Dept. of Physics, University of Nevada, Reno, NV 89557.

II. BACKGROUND

A. Two-photon decay

Hydrogenlike atoms. Breit and Teller [7] were the first to estimate the decay rates of the low-lying levels of hydrogen and helium. They confirmed the prediction by Göppert-Mayer that the H-like $2\,^2S_{1/2}$ state in hydrogen decayed primarily by emission of two electric-dipole ($2E1$) photons. Accurate nonrelativistic calculations for the dominant $2E1$ decay mode of the $2\,^2S_{1/2}$ state of one-electron atoms have been made by Spitzer and Greenstein [4], Shapiro and Breit [8], Zon and Rapoport [9], Klarsfeld [10,11], and Drake [12]. Au [13] studied the effect of including higher multipoles in the calculation and found that this gives rise to an asymmetry about $\theta = 90°$ in the angular correlation between the two photons of order $(\alpha Z)^2$. Tung *et al.* [14] studied two-photon decay between arbitrary states (n,l,m) of hydrogenic systems, and Florescu and co-workers [15,16] made a systematic study of $ns \rightarrow 1s$ and $nd \rightarrow 1s$ two-photon transitions.

Heliumlike atoms.. Dalgarno and co-workers [17,18] made the first calculation of the two-photon decay rate of the $2\,^1S_0$ level for helium. Other nonrelativistic calculations for He-like atoms have been done by Victor and co-workers [19,20], Jacobs [21], and Drake and co-workers [12,22].

Although the $1s2s\,^3S_1$ level decays predominantly by single-photon $M1$ emission, it has a small branch to decay via two photons. This process has been analyzed by Bely and Faucher [23,24] and by Drake and co-workers [22,25]. Bely and Faucher's results extend from $Z = 2$ to 31. The branching ratio for double-photon decay is small throughout this range, the largest value is 5×10^{-4} for $Z = 31$. The continuum radiation in this case has a markedly different spectral shape compared to the decay of the $2\,^1S_0$ state or the H-like $2\,^2S_{1/2}$ state. It is zero at the midpoint where the two photons would share the transition energy equally and peaks near each endpoint. The angular distribution in the opening angle θ has the form $1 - \frac{1}{3}\cos^2\theta$, which has a maximum at $\theta = 90°$ in contrast to the angular distribution for decay of the $2\,^1S_0$ level which has maxima at $\theta = 0°$ and $180°$. The $2\,^3P_0$ level in He-like ions can also decay by emission of two photons. This process involves both $E1$ and $M1$ couplings and it becomes important at high Z. Drake [26] calculated the $E1M1$ transition probability for decay of the $2\,^3P_0$ level at $Z = 92$, and found that this state decays 30% of the time via emission of two photons. This transition has been discussed in connection with measurement of parity nonconservation in high-Z heliumlike ions [27]. Schmieder [28] discussed double- and triple-photon decay of the $2\,^3P_0$ level in Be-like ions. To date, none of these exotic decay modes of triplet He- and Be-like ions has been observed.

Lifetime measurements Two-photon decay was first observed unambiguously by Novick and co-workers [29–31], who detected coincident vacuum ultraviolet photons from decay of the $2\,^2S_{1/2}$ level of He$^+$. Since the initial observations, most of the studies of two-photon decay have aimed at measuring the lifetimes of the two-photon-emitting states. The lifetime of the $2\,^2S_{1/2}$ level in H-like ions has been measured for a number of ions in the range $Z = 1$–47 [32–42], with results at the level of 1% being reported for Ar^{17+} [35] and Ni^{27+} [32]. The lifetime of the $2\,^1S_0$ level in He-like ions has been measured for ions from $Z = 2$ to

41 [5,6,32,33,35,41–45]. The most precise measurements have been made in Kr^{34+} [6], Br^{33+} [5], and Ni^{26+} [32], where uncertainties of about 1% have been reported.

Inner-shell vacancy states Two-photon transitions between inner-shell vacancy states in neutral atoms were first studied theoretically by Freund [46]. He found that the branching ratios were about 10^{-6} of the single-photon transition probabilities, and suggested that these decays might be observable. In summing over intermediate states in his calculations, he did not include the occupied bound states of the atom. Following this work, a number of theoretical studies, both nonrelativistic [47–50], and relativistic [51,52], have been reported. Guo [53] proved that the Pauli exclusion principle does not prohibit summing over all intermediate states including occupied bound states. If such occupied states lie between the initial and final states (e.g., the $2p$ state in the two-photon transition $3d \rightarrow 1s$) then there is a large increase in the differential transition probability (''intermediate-state resonance'') when the energies of the photons approach the values of a cascade decay via these levels.

Bannett and Freund were the first to observe two-photon decay from inner-shell-vacancy states [48,54]. Vacancy production was produced by irradiating a thin Mo foil with Ag x rays from a sealed x-ray tube. Identification of the two-photon-decay mode was achieved by observing coincidences between a pair of Si(Li) detectors. They observed both $2s \rightarrow 1s$ and $3d \rightarrow 1s$ decays in molybdenum. The continuum shape was observed over a restricted energy range near the midpoint of the distribution. The data for the $3d \rightarrow 1s$ decay were consistent with the expected intermediate-state resonance.

Ilakovac and co-workers [55–57] studied two-photon decay of inner-shell vacancies in xenon, silver, and hafnium atoms. They used radioactive sources to generate the inner-shell vacancies, and identified the decays using a pair of high-purity germanium detectors. Two-photon emission in the transitions $2s \rightarrow 1s$, $3s \rightarrow 1s$, $3d \rightarrow 1s$, and $4sd \rightarrow 1s$ were observed and compared with the various theoretical calculations. They found general agreement with the expected continuum shapes and, in particular, the single-photon spectra of the $3d \rightarrow 1s$ transitions in silver and hafnium showed minima at the midpoints of the distributions, and rose for increasingly asymmetric energy partition between the two photons. This was a clear confirmation of the predicted intermediate-state resonance effect, and supported Guo's assertion about the need to include the occupied levels in the sum over the intermediate states. If the occupied states (in particular, the $2p$ states) are not included in the sum over intermediate states, the calculation of the transition probability exhibits a maximum at the midpoint of the distribution [57].

Nuclear gamma decay. Two-photon emission has also been observed in nuclear transitions in ^{40}Ca, ^{90}Zr [58], and ^{16}O [59] using the Heidelberg-Darmstadt ''crystal ball'' which is a 4π array consisting of 162 NaI(T1) γ-ray detectors. A surprising result of this research was that, in each case, the angular correlation between the two γ rays was asymmetric about $90°$. This was interpreted as arising from interference between the $2E1$ and the $2M1$ contributions to the transitions which were found to be of comparable strength. The theory of nuclear 2-γ decay including treatment of higher multipolarities and angular correlations is dis-

cussed in an appendix to Ref. [59]. The nuclear experiments generally confirmed the expected continuum spectra from 2-γ coincidences, but the interpretation was complicated by a large background of events associated with the internal pair conversion (IPC) decay mode [60,61] of the nuclear states. Positron annihilation in flight following IPC produced coincidence events which, in certain kinematic regions, were indistinguishable from 2γ decays.

B. Shape of the 2γ continuum in H-like and He-like ions

Among the remaining experimental issues in the study of two-photon decay is a detailed examination of the shape of the two-photon continuum in simple one- and two-electron ions. These systems have states which decay predominantly by emission of two photons, so that clean, high-precision experiments are possible. The theoretical calculations predict that the spectral distributions should depend on the nuclear charge, but this has not been verified.

The two-photon differential decay probability can be written (in atomic units) [62],

$$\frac{dw_{2\gamma}}{d\omega_1} = \frac{\omega_1\omega_2}{(2\pi)^3 c^2}|M_{2\gamma}|^2 d\Omega_1 d\Omega_2, \qquad (1)$$

where ω_j is the energy, and $d\Omega_j$ is the solid angle for the jth photon. The transition energy ω_0 satisfies $\omega_0 = \omega_1 + \omega_2$. The second-order matrix element $M_{2\gamma}$, after summation over magnetic quantum numbers, has the form

$$M_{2\gamma} = \hat{\boldsymbol{\varepsilon}}_1 \cdot \hat{\boldsymbol{\varepsilon}}_2 \sum_n \left[\frac{\langle 1\,^1S_0\|R_{E1}(\omega_2)\|n\rangle\langle n\|R_{E1}(\omega_1)\|2\,^1S_0\rangle}{E_n - E_{2\,^1S_0} + \omega_1} \right.$$
$$\left. + \frac{\langle 1\,^1S_0\|R_{E1}(\omega_1)\|n\rangle\langle n\|R_{E1}(\omega_2)\|2\,^1S_0\rangle}{E_n - E_{2\,^1S_0} + \omega_2} \right]. \qquad (2)$$

Here $\hat{\boldsymbol{\varepsilon}}_j$ is the polarization vector for the jth photon, E_n is the energy of the intermediate state n, and $R_{E1}(\omega_1)$ is the operator for electric dipole emission. The summation is over the complete set of intermediate states including the positive- and negative-energy continua. Apart from a trivial factor arising from the two-photon phase space, the shape of the two-photon continuum emission is determined by the matrix elements and energy denominators appearing in the summation in Eq. (2).

One-electron atoms. Klarsfeld's nonrelativistic result for decay of metastable hydrogenic atoms ($2\,^2S_{1/2}$ level) after averaging over photon polarization is [10,11],

$$\frac{d^3W}{dE_1 d\Omega_1 d\Omega_2} = Z^4 \alpha^6 \frac{2^5}{(2\pi)^3 3^8}(1+\cos^2\theta)y(1-y)\phi^2(y),$$
$$(3)$$

where θ is the angle between the two photons, Z is the nuclear charge, and y is the fraction of the transition energy $E_0 = E_1 + E_2$ carried by one of the photons. The function $\phi(y)$ is given by

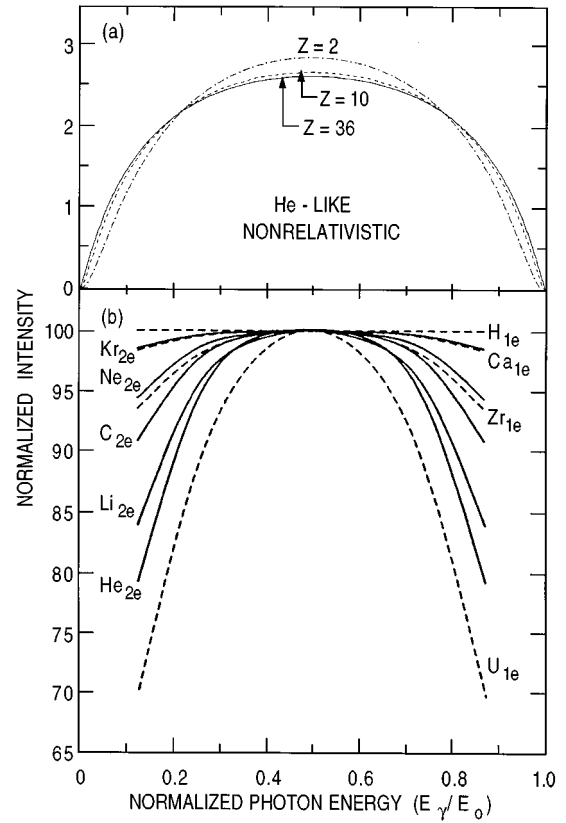$$\phi(y) = Q(2(1+3y)^{-1/2}) + Q(2(4-3y)^{-1/2}), \qquad (4)$$

where

FIG. 2. Spectral distributions for two-photon decay for various values of the nuclear charge Z. (a) $2\,^1S_0$ level in He-like ions. These curves are normalized to give an area of 2. (b) Comparison of spectral distributions in the two-photon decay of the $2\,^2S_{1/2}$ level in H-like ions (dashed curves) and the $2\,^1S_0$ level in He-like ions (solid curves). These curves are normalized to the shape of the two-photon continuum for the $2\,^2S_{1/2}$ level of atomic hydrogen.

$$Q(\xi) = 3\xi(\xi-2)^{-1} + 2(\xi-1)(3-\xi)^{-1}$$
$$\times F(5,1;4-\xi;(\xi-1)(2-\xi)/6\xi), \qquad (5)$$

and $F(a,b;c;z)$ is the Gauss hypergeometric function. Equation (3) indicates that, in the nonrelativistic limit, the spectral shape for double-photon decay of the H-like $2\,^2S_{1/2}$ state does not depend on Z. The nonrelativistic decay rate is obtained by integrating Eq. (3) over angles and energy. The most recent calculation by Drake [12] gives

$$W_{NR}^{2\,^2S_{1/2}\,2E1} = 8.229\,38Z^6\ \mathrm{s}^{-1}. \qquad (6)$$

Parpia and Johnson [63,64] and Goldman and Drake [62,65] have made fully relativistic calculations of the H-like decay rate. Johnson [63] presents a tabulation of the frequency distribution $\psi(y,Z)$ (in terms of the Rydberg frequency Ry) defined by

$$\frac{dW_{\mathrm{rel}}^{2\,^2S_{1/2}\,2E1}}{dy} = Z^6(9\alpha^6/2^{10})\psi(y,Z)\ \mathrm{Ry}. \qquad (7)$$

Some of these results are plotted in Fig. 2(b). Relativistic corrections give rise to a dependence of the shape on Z.

Heliumlike atoms. For heliumlike atoms there have been no fully relativistic calculations of the two-photon decay rate. However, in this case, the shape of the two-photon continuum varies with Z, even in the nonrelativistic limit. This is because of the effect of the electron-electron correlations. The Z dependence of the shape is illustrated in Fig. 2(a) which shows some of Drake's results [66] for the continuum shape between $Z=2$ and 36. In Fig. 2(b) a comparison of the shapes of two-photon decays in H- and He-like ions is presented.

It is interesting to note the opposite behavior of the shapes of the H- and He-like results as a function of Z. As can be seen in Fig. 2(b) the shape for one-electron ions becomes more sharply peaked as Z increases while in the case of two electron atoms, the shape is most sharply peaked for helium ($Z=2$). This behavior is related to the difference in the scaling of the energy separations within the $n=2$ shells of these atoms. For the He-like case (at low Z) the energy separation is dominated by the electron-electron interaction and has a linear increase as a function of Z. For H-like ions the $2s$-$2p$ energy separations scale as Z^4 due to relativistic and quantum electrodynamic effects. The energy separations $2s$-np scale roughly as Z^2 in both species. So neglecting the matrix elements, the relative importance of the $2s$-$2p$ coupling increases in He-like ions as Z increases since $\Delta E(n=2)/\Delta E(n>2)\approx 1/Z$, whereas the $2s$-$2p$ coupling becomes less important for H-like ions as Z increases since for these ions $\Delta E(n=2)/\Delta E(n>2)\approx Z^2$. Although the He-like continuum shape has not been calculated for ions heavier than $Z=36$, one might expect a reversal in very heavy He-like ions giving rise to a sharper peaking at high Z since relativistic corrections become more important than electron-electron interactions in these ions.

C. Experimental observations of two-photon continuum emission

The first observation of the continuum emission from He-like ions was made by Elton, Palumbo, and Griem [67]. They observed a deuterium-neon plasma using a 2.2-m grazing-incidence grating spectrometer. The detector was a photographic plate. A broad peak near 36 Å was present when neon was added to the plasma. The width and position of this feature agreed with that expected for the two-photon continuum of Ne IX (in second order). The intensity was comparable to that of the background continuum. Strong lines from H- and He-like impurities were superposed on the broad feature.

Rough verification of the shape of the continuum radiation from decay of metastable H-like atoms was made by Lipeles, Novick, and Tolk [30] using He^+ and by O'Connell *et al.* [68] using hydrogen. They used photomultiplier tubes fitted with interference filters to survey the continuum shape. They also measured the opening angle between the photons demonstrating the $(1+\cos^2\theta)$ angular correlation.

Marrus and Schmieder [33,69] used the beam-foil technique to study two-photon decay in highly charged ions. They observed the continuum radiation from decay of the $2\,^2S_{1/2}$ level in H-like argon and the $2\,^1S_0$ level in He-like argon using a pair of lithium-drifted silicon [Si(Li)] detectors. This method has also been used to observe the two-

photon continuum in H-like Ni [41], Kr [39], and Nb [42], and He-like Ni [41], Br [5], Kr [6], and Ag [42]. These experiments resulted in measurements of the lifetimes of the two-photon-emitting states, but detailed measurements of the shapes of the continua were not attempted. The continuum radiation from double-photon decay was also observed in connection with studies of resonant transfer and excitation in He-like Ge [70], and Kr [71–73]. These experiments pointed to a technique for selective excitation of the $2\,^1S_0$ level in He-like ions which could be important in future studies.

The experimental conditions in our Br lifetime measurement [5] were not optimum for measuring the shape of the 2γ continuum radiation. One reason was that, in that experiment, intense low-energy lines were blocked using mylar absorbers. This was necessary in order to reduce the accidental coincidence rate, but it also restricted the range over which we could observe the two-photon continuum. In addition, much of the integration time in that experiment was spent with the foil at large distances from the detectors (i.e., many decay lengths) where the two-photon rate was low. So, a dedicated experiment was needed to measure the continuum shape. In planning this experiment, an effort was made to maximize the sensitivity to low-energy x rays, and the foil position and detector geometry were chosen to optimize the two-photon-coincidence rate. The goal of this work was to measure the shape with sufficient detail to challenge theoretical calculations.

III. EXPERIMENT

The experiment consisted of two separate runs at the Argonne Tandem Linear Accelerator System (ATLAS). The experimental method was the same in the two runs but some improvements were made to the apparatus prior to the second run. Since the experimental setup in the first run is discussed in published conference proceedings [74], this paper will focus on the second run.

After acceleration to 708 MeV, the ^{84}Kr ions were stripped in a 200-$\mu g/cm^2$ carbon foil, and the 34+ charge state (about 16% of the total beam) was magnetically selected and directed to our target chamber. The beam pulses were separated by 82.5 ns, and were about 1 ns wide at our target position. In the target chamber (see Fig. 3), the ions were excited by a 10-$\mu g/cm^2$ carbon foil (The final beam energy was 701 ± 8 MeV following energy loss in the foils.) The region of the beam downstream of the foil was viewed by three Si(Li) x-ray detectors. A ''shield'' consisting of a thin molybdenum sheet with an 8-mm aperture for the beam was placed downstream of the target. This shield, together with molybdenum masks placed over each detector, prevented detection of the intense flux of x rays coming directly from the target. The foil and the shield were attached to a translation stage which could be accurately positioned relative to the detectors. Not shown in the diagram is an insertable Faraday cup fitted with a 2-mm aperture which could be placed at the target position and was used for the initial beam tuning and to monitor the beam position during the run. During tuning, the transmission through this aperture was maximized and typically 90% transmission was achieved. A fixed 4-mm aperture located 10 cm upstream of the target served to clean up any beam halo. The current on this aperture was
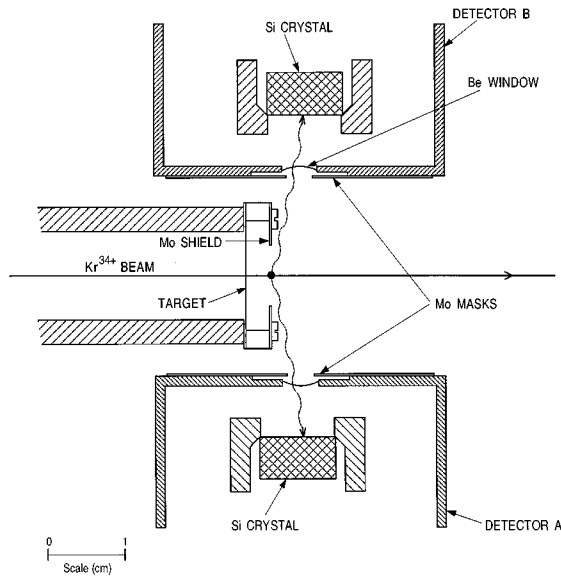
FIG. 3. Experimental setup with target foil at the "normal position." See also Table I. The center line of detector C (not shown) was perpendicular to the beam and to the center lines of detectors A and B.

read and minimized during tuning and then checked periodically during the measurement. Before each run the positions of all detectors, masks, and the target stage were determined to better than 0.5 mm. Some of the relevant positions are given in Table I.

The preamplifier output from each detector was sent to three amplifiers: (1) an "energy" amplifier with a shaping time of 6 μs, (2) a "slow" timing amplifier with a shaping times of 2 μs, and (3) a "fast" timing amplifier with a shaping time of 0.25 μs. The output of the energy amplifiers were routed to a peak sensing analog-to-digital converter. The outputs of the fast and slow timing amplifiers were sent to discriminator circuits to produce timing pulses. Coinci-

dences between these two pulses produced "fast-slow" timing signals which were used to gate the electronics, measure the time differences between the detectors, and detect pileup. The fast-slow timing was required in order to obtain timing information for photons with energies less than 1 keV, while simultaneously minimizing electronic dead time. The pulse height corresponding to 1 keV was below the noise level of the fast amplifier so the rate of fast timing pulses rose rapidly as the discriminator was set to accept pulses corresponding to energies of less than 1 keV. For example, the rate was 5–10 kHz with the discriminator set to accept 800-eV photons. By contrast, the noise level in the slow-timing amplifier was well below the pulse height corresponding to 800-eV photons. In the fast-slow timing scheme, the time of arrival of a signal is determined by the fast-timing pulse but the fast-slow coincidence condition eliminates the pulses generated by electronic noise.

If two photons entered one of the detectors within 20 μs, this was considered a "pileup" event. For such events, the energy measurement for the detector was suspect since the two pulses were combined in the energy amplifier which had a long shaping time. The shaping time was set to optimize the energy resolution. In order to maintain the best resolution while minimizing the pileup problem, we used pileup detection circuitry to flag such events. These could then be examined and then eliminated in the data analysis. If the pulses were closer than about 2 μs, the event was not flagged as a pileup since the fast-slow timing only produced one pulse. This minimum was essentially set by the time constant of the slow-timing amplifier.

In our experiment, a "coincidence" was defined as an event in which the fast-slow timing pulses for any two detectors arrived within 1 μs of each other. For these events, all the measured parameters were written to tape and sorted with an on-line data-analysis program. We also recorded a small fraction of "singles" events in which only one of the detectors fired. The fraction of singles events recorded was adjusted individually for each detector by setting a parameter N on a divide box which generates one output pulse for every N input pulses. We adjusted the divide boxes so that

TABLE I. Detector geometry and other experimental parameters (first run).

	Detector A	Detector B	Detector C
Detector dimensions (mm):			
Active diameter (Si crystal)	9.7	9.7	6.2
Sensitive depth (Si crystal)	5.33	5.15	5.27
Mask dimension[a]	5 by 3.5	5 by 3.5	12.7 by 4
Crystal position:[b]			
x	-0.3 ± 0.1	-0.2 ± 0.1	
y	21.43 ± 0.2	-21.33 ± 0.2	
z	3.75 ± 0.1	4.45 ± 0.1	
Mask position[c]	13.13 ± 0.1	-13.03 ± 0.1	21.18
Other parameters:			
Target to shield distance	3.38 ± 0.1 mm		
Beam energy[d]	797 ± 8 MeV		

[a]The shorter dimension is parallel to the beam direction.

[b]Position of crystal font face relative to center of shield. The beam travels along z, and the y axis is normal to the crystal faces for detectors A and B. See Fig. 3. The x axis is normal to the crystal face for detector C.

[c]y coordinate for detector A and detector B, x coordinate for detector C.

[d]The beam energy was 701 ± 8 MeV in the second run.
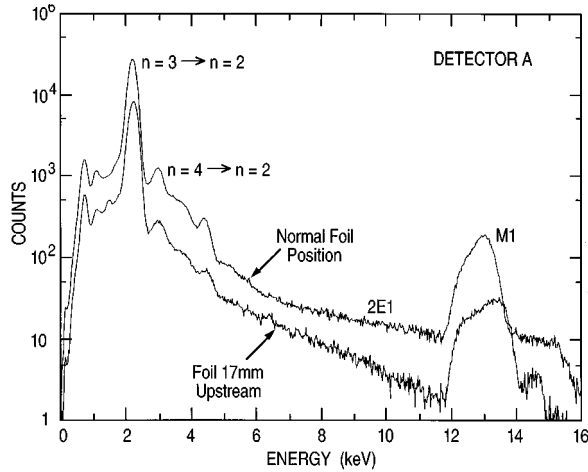
FIG. 4. Typical spectra measured using detector A with a beam of Kr^{34+} ions incident on a 10-$\mu g/cm^2$ target for the foil at the normal position (See Fig. 3), and moved 17-mm upstream. In the second run, singles rates in detectors A and B were typically 4 kHz at the normal foil position.

FIG. 5. Electronic efficiency measurements for detector A. Ratio of pulser counts to x-ray counts as a function of the ''energy'' of the pulser peak. The solid line is a fit to a Woods-Saxon-type function used for interpolation.

the rate of coincidences and singles were comparable.

A typical x-ray spectrum measured in the Si(Li) detectors is shown in Fig. 4. The line at about 13 keV comes from single-photon decays from the $n=2$ levels of He-like krypton which were mostly due to $M1$ decay of the $2\,^3S_1$ level. The strong line at 2.2 keV is due to decays from $n=3$ to $n=2$ in He- and Li-like ions. Other transitions into $n=2$ are seen at higher energies. The two-photon continuum is most cleanly seen in the region to the low-energy side of the $M1$ peak but there are other contributions to this region such as tails of the single-photon lines, scattered x rays, and backgrounds from nuclear processes.

A multichannel time-to-digital converter was used to measure the time of arrival of the detector signals relative to a reference from the accelerator $\sim$12-MHz pulse structure. These data were used to determine time differences between the detector signals. The time resolution varied with the energy of the photons and was worse than that obtained in our earlier work on Br (Ref. [5]) and Ni (Ref. [41]). The reason was the requirement to maximize the efficiency for detecting low-energy photons which required longer time constants in the fast timing amplifiers to pull small signals out of the noise. Coincidence events in which the two photons shared the transition energy equally had better time resolution than asymmetric events which involved low-energy photons.

Understanding the efficiency of our photon-counting electronics as a function of energy was important in this experiment. A key issue was the ability of low amplitude pulses to trigger the discriminators. To measure this we simultaneously recorded signals from a variable electronic pulser and 6.4-keV x rays produced by a ^{57}Co radioactive source. We then determined the ratio of counts in the pulser peak to counts in the 6.4-keV peak as a function of pulser amplitude. A typical result for detector A is shown in Fig. 5. This information was used as one of the inputs to the Monte Carlo simulation program discussed in Sec. V. By means of the fast-slow timing technique, it was possible to set the thresholds low enough to obtain unit electronic efficiency down to about 1.2 keV in all three Si(Li) detectors.
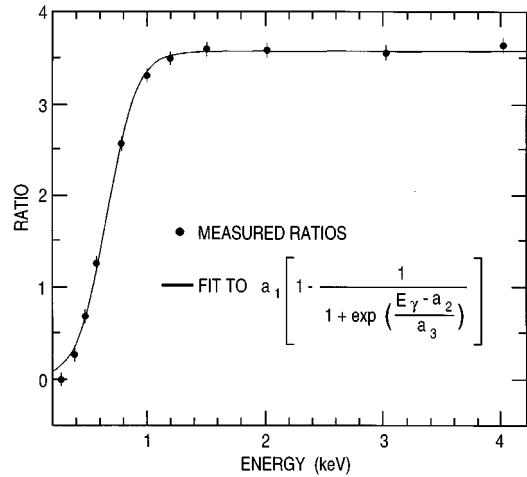
IV. DETECTION EFFICIENCY

Characterization of the efficiency of the detectors as a function of energy was crucial in this experiment. Absolute efficiency calibration of Si(Li) x-ray detectors has been discussed by Hansen *et al.* [75], Alfassi and Nothman [76], Cohen [77–79], Campbell and McGhee [80], and Shima *et al.* [81]. For our detectors the thicknesses of the silicon crystals were sufficient to completely absorb x rays in the energy region of interest (0.8–14 keV), so the efficiency was dominated by the absorption of x rays in various materials located between the source of emission and the active portion of the detector. A list of the absorbing layers for our detectors is given in Table II. Additional absorption could be caused by the buildup of ice [78] on the cooled surface of the detector. Other processes which affect the detection efficiency include incomplete conversion of the x-ray energy and escape of silicon characteristic x rays. The probability for escape of a silicon K x ray increases with decreasing x-ray energy down to the silicon K edge. Cohen [77] found the ratio of the silicon escape peak to the photopeak increased from 0.14% at 8.6 keV to 0.8% at 3.7 keV. This is in rough agreement with the size of the escape peaks observable in our calibration spectra.

TABLE II. Detector characteristics.

	Detector A	Detector B	Detector C
Absorbing layers (μm):			
Be window	8 ± 2	8 ± 2	25.4
Au layer	0.022 ± 0.003	0.018 ± 0.003	0.02
Inactive Si layer	0.5 ± 0.2	0.5 ± 0.2	0.1
Ice	0^{+2}_{-0}	0^{+2}_{-0}	0
Energy resolution [a]			
σ_0^2 (keV^2)	0.008 66	0.005 24	0.004 73
σ_E^2 (keV)	0.000 45	0.000 48	0.000 41
$\sigma(E_0)$ (keV)	0.121	0.107	0.100

[a]See Eq. (8) for second run.

TABLE III. Sources used in the efficiency and energy calibrations.

Source	X ray	Energy (keV)	$I(\text{x ray})/I_\gamma$
^{109}Cd	L	3.1	2.94 ± 0.34
^{54}Mn	K_α	5.412	0.2234 ± 0.0011
	K_β	5.95	$0.0305 \pm 0.000\,34$
^{57}Co	K_α	6.397	0.5863 ± 0.016
	K_β	7.06	0.0807 ± 0.0024
^{65}Zn	K_α	8.041	0.6790 ± 0.0044
	K_β	8.91	$0.0946 \pm 0.000\,77$
^{85}Sr	K_α	13.375	0.5035 ± 0.0035
^{88}Y	K_α	14.142	0.5425 ± 0.0035
^{57}Co	γ ray	14.41	0.1086 ± 0.0023
^{85}Sr	K_β	14.96	0.089 ± 0.00077
^{88}Y	K_β	15.84	$0.0986 \pm 0.000\,81$
^{109}Cd	K_α	22.1	22.47 ± 0.58
^{113}Sn	K_α	24.14	1.225 ± 0.009
^{109}Cd	$K_{\beta'_1}$	24.93	4.022 ± 0.107
	$K_{\beta'_2}$	25.46	0.706 ± 0.023
^{113}Sn	$K_{\beta'_1}$	27.27	0.220 ± 0.005
	$K_{\beta'_2}$	27.86	$0.0414 \pm 0.000\,87$
^{139}Ce	K_α	33.30	0.792 ± 0.011
	$K_{\beta'_1}$	37.8	0.151 ± 0.004
	$K_{\beta'_2}$	38.7	0.0388 ± 0.0009

FIG. 6. Detector efficiency vs photon energy for detector A. Data points are absolute efficiency measurements made using open radioactive sources whose intensities had been determined from γ-ray measurements. The solid line is a fit to the thicknesses of the various absorption layers.

We followed the method described by Campbell and McGhee [80] to determine the efficiency of our detectors. A number of open radioactive sources were made and their intensities were calibrated by counting gamma rays in a germanium detector whose absolute efficiency was measured by established techniques. We then used the conversion factors from Ref. [80] to convert the γ-ray intensities to x-ray intensities for the calibration lines listed in Table III. In a series of measurements done immediately following our first run, we measured each of the sources and determined the absolute efficiencies of detectors A and B at each calibration point. (The absolute efficiency of detector C was not determined. This detector was used only for diagnostic purposes.)

Applying the Monte Carlo simulation (discussed in Sec. V) to the source measurements, and varying the absorber and crystal thicknesses in the program, we arrived at a set of parameters that gave good agreement between the efficiency-calibration data and simulation (see Fig. 6). This procedure allowed us to represent the efficiency in terms of a few physical parameters describing the detectors, and also allowed us to extrapolate the efficiency curves to regions that were not measured, such as below 3.1 keV.

Separate measurements were done to determine the thicknesses of the silicon dead layers and the gold layers. These were important parameters for understanding the detector efficiencies at low energy, and the independent determination allowed us to constrain these thicknesses in the final fits to the efficiency calibration data. For the silicon dead layer, we used a method suggested by the work of Shima *et al.* [81]. This involved studying the line shape produced when a monoenergetic x ray was detected. The ratio between the counts in the low-energy tail and the counts in the peak were related to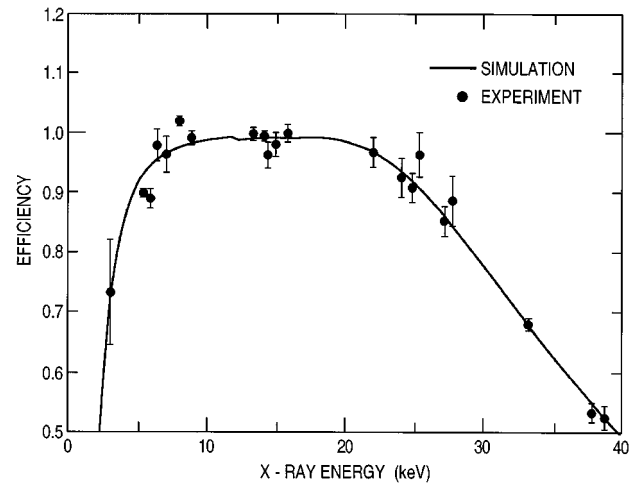 the thickness of the silicon dead layer and the known absorption cross section in silicon for an x-ray of that energy [82]. Monoenergetic lines of Cu and Cr were obtained using an x-ray tube followed by a crystal monochromator. Our results for the silicon dead layer thicknesses are given in Table II together with the values of other parameters determined from the efficiency measurements. To measure the thickness of the gold contact layer, the calibration data obtained using the ^{85}Sr source were used. We measured the intensity of the gold L x-ray peaks appearing on the low-energy side of the K x-ray lines of Rb emitted by the source. The thickness of the gold was then determined from the ratio of the intensities of the Au and Rb lines in the spectrum and the known photoabsorption cross sections for Au. The results of this analysis are also given in Table II.

V. MONTE CARLO SIMULATIONS

We developed a Monte Carlo simulation [83] of the Kr shape-factor experiment which allowed us to make detailed comparisons between our measurements and theoretical calculations. Careful measurements were made of the geometry of the detectors (by x-ray photography) and target chamber (through optical techniques) to provide data for the program. Other input data included the beam velocity, thicknesses of the absorbing layers, electronic efficiencies, energy-dependent widths of x-ray lines, detector calibration constants, and x-ray mass attenuation coefficients. Some of these data are presented in Tables I and II. The detector efficiency determination was discussed in Sec. IV. For the energy calibrations we used the radioactive sources listed in Table III. Data were taken with these sources before and after each run, and the centroid of each peak was determined using a least-squares Gaussian-peak-fitting program. The calibration constants for each detector were then determined by a least-squares fit to the line energy vs centroid data. The radioactive sources were also used to determine the energy dependence of the detector linewidths. These were fit to the relation:

$$\sigma = \sqrt{\sigma_0^2 + E_\gamma \sigma_E^2}, \qquad (8)$$

where σ is the standard deviation for the Gaussian shape, and E_γ is the x-ray energy. The parameters σ_0^2 and σ_E^2 were determined by fitting the source data to Eq. (8).

The ion beam velocity was determined by a time-of-flight energy measurement system located in a long drift section just after the accelerator. This system is described in Ref. [84]. In order to determine the exact locations of the silicon crystals and collimators, we made radiographic images of the internal structure of the detectors.

For each simulated event in the Monte Carlo program, the first photon is generated isotropically, while the second is distributed with an angular correlation of $1 + \cos^2\theta$. The energy of the first photon is chosen from a given theoretical two-photon decay distribution while the second photon is determined so as to conserve energy for the transition. The decay point in the target chamber is chosen assuming an exponential decay along the beam path with a specified lifetime and ion velocity. Decay points are also spread in the transverse direction with a Gaussian distribution. For each photon generated, the program tests to see if it is blocked by the shield, and then checks each detector to see if the photon could reach its silicon crystal and, if so, computes the photon trajectory through the crystal volume. For every ''hit'' the photon energy is Doppler corrected, and a determination is made as to whether it is lost in an absorbing layer or passes through the crystal without being detected. The program also tests whether a silicon x ray escapes from the crystal (and appropriately adjusts the absorbed energy), is lost due to the inefficiency of the electronics, or is lost due to incomplete charge collection. If both photons pass all of these tests, the event is accepted and a pulse height is assigned to each photon according to the resolution function for the corresponding detector. A similar procedure is applied to analyze single-photon events. In either case, the distributions generated by the program can be compared directly with the experimental data.

In order to check the operation of the program and fine tune the input parameters in a manner independent of the two-photon decays, we simulated events from the $M1$ decay of the $2\,^3S_1$ level in He-like Kr. This transition gives a line at about 13 keV which is prominent in Fig. 4. It is broadened because of the Doppler shifts along the relatively long decay path and thus provides a good test of the experimental geometry. During each experimental run, we took some data with the foil moved upstream by 17 mm. From previous experiments [85], we knew that most of the counts in the 13 keV line at this foil position were due to the $M1$ decays. We then slightly adjusted the parameters describing the geometry of the interaction region to optimize the agreement between the $M1$ data (line shapes and relative count rates) and the Monte Carlo results. These adjustments were of the order of magnitude of the errors in the parameters listed in Table II. In Fig. 7 a comparison between the $M1$ line shapes determined by the experiment and by the simulation is presented. As can be seen, good agreement was obtained, and this provided some assurance that the Monte Carlo program was working properly.
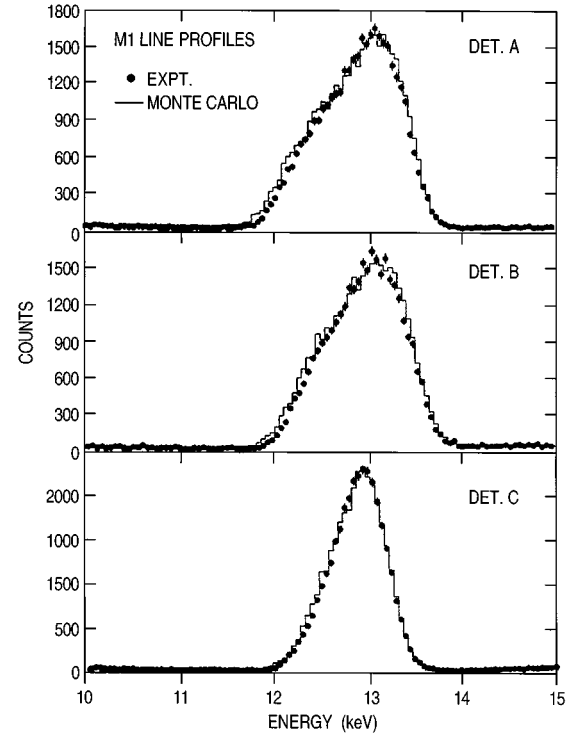

FIG. 7. Monte Carlo simulations of the line shapes for the $M1$ decay of the $2\,^3S_1$ level in He-like Kr (solid lines). The data points were taken with the foil located 17 mm upstream of the normal position.

VI. RESULTS AND DISCUSSION

The measurement of the spectral shape of the two-photon continuum was based on the data obtained from detectors A and B. Detector C was used mainly in the tests of the operation of the Monte Carlo simulation discussed in Sec. V. It was clear from the x-ray spectra measured by the individual detectors (see Fig. 4) that, in order to separate the two-photon continuum from other background processes, we needed to use coincidence techniques. Figure 8 is a time-difference spectrum for coincidences between detectors A
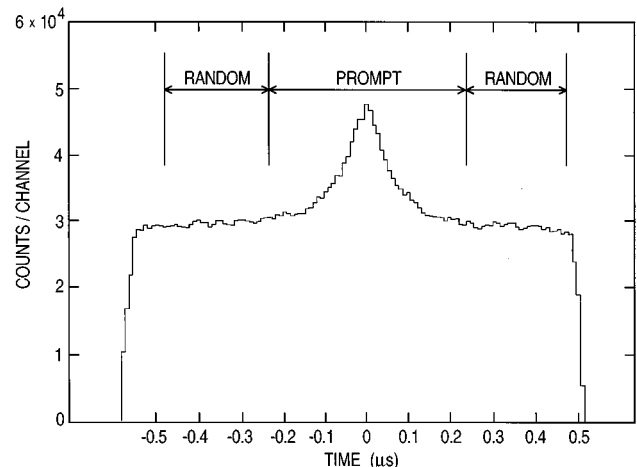

FIG. 8. Time-difference spectrum for coincidences between detectors A and B. The prompt and random windows were used in the analysis of coincidence events.
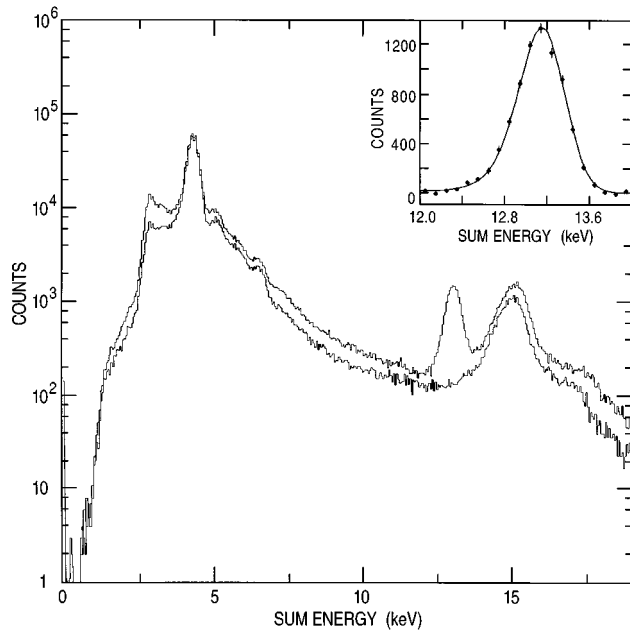
FIG. 9. Sum-energy spectra for prompt and random coincidences with the foil at the normal position. Inset includes a Monte Carlo simulation of the sum-energy peak from two-photon decay. The data (solid dots with errors in the inset) were cut on a wide region of the two-photon continuum in detector A.

and B. The peak labeled ''prompt'' corresponds to events originating from the same beam pulse and these are composed of both true and accidental coincidences. The regions labeled ''random'' are coincidences between photons originating from different beam pulses. The windows indicated in Fig. 8 were used to cut the data and separately analyze the prompt and random coincidences. The total width of the random windows is equal to the width of the prompt window.

Adding the energies measured with detectors A and B we obtain the ''sum-energy'' spectra shown in Fig. 9. The upper spectrum indicates the prompt coincidences, and the lower spectrum indicates the random coincidences. The events in the peak at a laboratory energy of 13.15 keV in the prompt spectrum are the two-photon decays. No peak appears at this position in the random spectrum, so we have a clear identification of the two-photon events. The inset is a comparison between the sum-energy peak measured in the experiment (points with errors) and the corresponding peak obtained from the Monte Carlo simulation (solid line).

The intense peak just below 5 keV in the sum-energy spectra in Fig. 9 arises from accidental coincidences between two Kr L x rays. The intensity of this peak is the same in both the prompt and random spectra. There is also a peak near 15 keV which corresponds to detection of an L x ray in one detector and an $M1$ photon in the other detector. This feature is mostly due to accidental coincidences, but there are some true coincidences here since there are more counts in the prompt spectrum. Similarly, some true coincidences occur in the continuum region, since there are more counts in the prompt spectrum. These true coincidence events can arise from cascade processes.

The correlation between the energies in detectors A and B for prompt- and random-coincidence events is given in the scatter plots of Fig. 10. The two-photon decays form a diag-
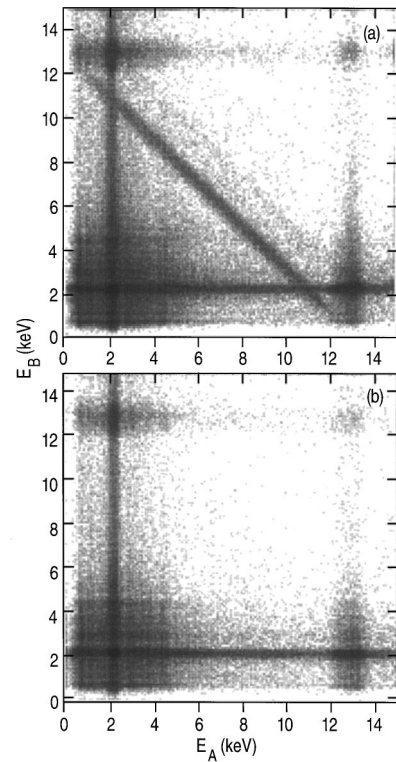

FIG. 10. Scatter plots (log scale) E_A vs E_B for (a) prompt coincidences, and (b) random coincidences.

onal stripe in the prompt coincidences [Fig. 10(a)] corresponding to a sum energy of $E_0 = E_A + E_B = 13.026$ keV. The horizontal and vertical stripes which occur in both scatter plots are coincidences involving a single-photon line in one detector, and continuum photons in the other detector. These are mostly random coincidences, but there are some true coincidences arising from events in which the single-photon line is part of a cascade into the two-photon-emitting state. We will refer to such events as ''cascade-continuum coincidences.''

Figure 11(a) is a projection of the diagonal stripe in the prompt-coincidence scatter plot [Fig. 10(a)] onto the E_A axis. The corresponding projection from the random plot is given in Fig. 11(b). Figure 11(c) is the difference between these two histograms, and corresponds to the ''true'' coincidence events. Figure 11(c) is a considerably cleaner spectrum of the two-photon-continuum region than the raw spectrum measured by detector A (see Fig. 4). However, these events are still not pure two-photon decays. Some of them are cascade-continuum coincidences which are part of the horizontal and vertical stripes in Fig. 10(a). At the point where these stripes intersect the diagonal stripe, the above analysis does not distinguish the cascade-continuum events from the two-photon-continuum events, so both of these appear in the true coincidences of Fig. 11(c). Because of this problem, a more involved procedure was used to extract the two-photon-continuum spectrum.

The procedure was based on a scatter plot (Fig. 12) comparing the sum-energy ($E_A + E_B$) to E_A. The two-photon-decay events form a vertical stripe at a fixed sum energy. We divided these data up into horizontal slices, each corresponding to a 400-eV-wide window of E_A. The slices are sum-energy spectra cut on E_A. Some of these are shown in Fig.
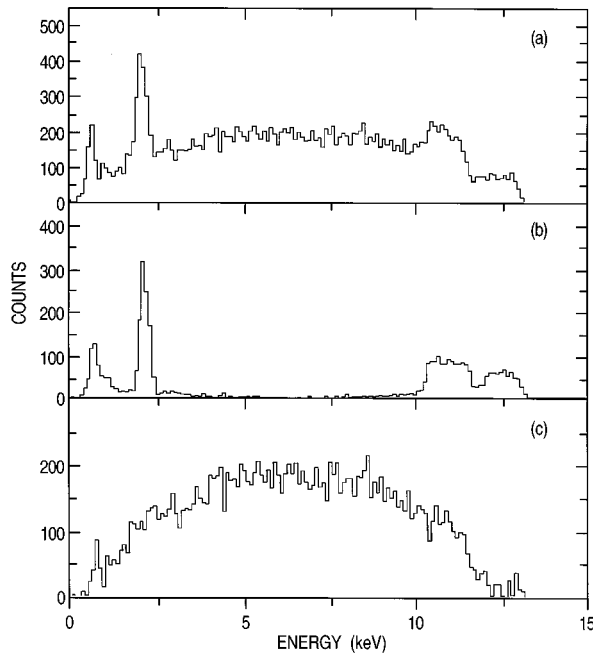
FIG. 11. Spectrum in detector A for events in the two-photon region of the sum-energy spectrum for (a) prompt coincidences and (b) random coincidences. (c) The difference between these giving the ''true'' coincidences.

13. We analyzed these spectra with a least-squares peak-fitting program incorporating Gaussian peak shapes and a quadratic background. The results for both runs are presented in Fig. 14(a), which gives the areas (data points and error bars) under the two-photon peaks as a function of E_A. Also shown are the 1σ errors in the areas as determined by the fitting routine. The curves are from Monte Carlo simulations of each run based on Drake's nonrelativistic [12,66] calculation for $Z=36$. (The slight structural variations near 11 and 2 keV are caused by the Si absorption edge.) It is seen that the data are well represented by the theory.

Note that the Monte Carlo results for the two experimental runs are nearly identical, so that the errors in the experimental points could be reduced by combining the data for the two runs. However, we did not do this. The reason is that the
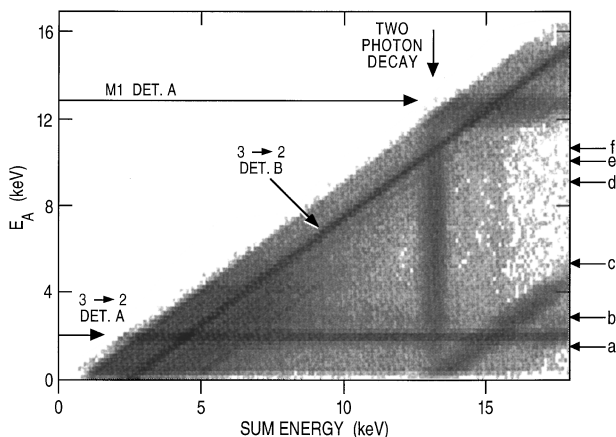

FIG. 12. Sum energy vs E_A for coincidences between detectors A and B. The arrows and letters in the right margin correspond to the spectra displayed in Figs. 13(a)–13(f).
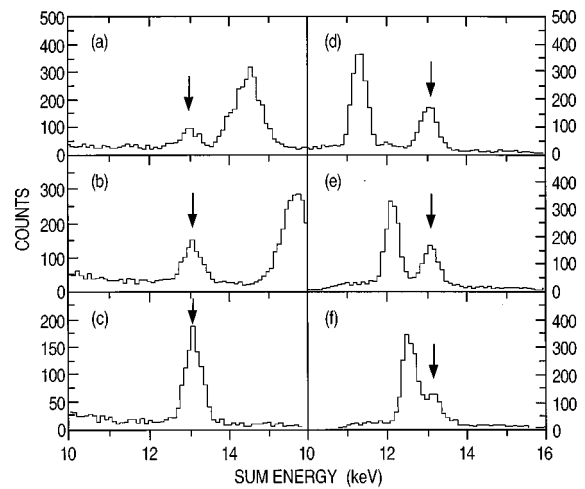

FIG. 13. Sum-energy spectra cut on a 400-eV-wide window in detector A centered at (a) 1.6, (b) 2.8, (c) 4.8, (d) 9.2, (e) 10, and (f) 10.4 keV.

backgrounds were considerably higher in the first run, as ions from the beam were hitting the shield (see Fig. 3). For the second run, we improved the beam diagnostics and focusing, and increased the diameter of the shield from 6 to 8 mm. These measures greatly reduced the backgrounds, so we believe the data from the second run are more reliable. Also, since the experiment was limited by uncertainties in the detector efficiencies, rather than by the statistical accuracy, we decided to base our final results on data from the second run. It is encouraging, however, that the results from the two runs are consistent, and that we were able to extract the two-
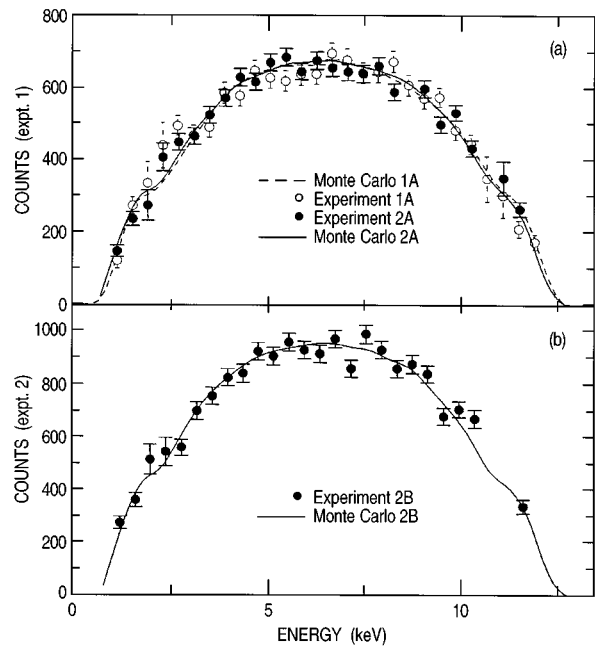

FIG. 14. Data points are counts determined from fitting the two-photon peaks in the sum-energy spectra cut on (a) detector A or (b) detector B. Open circles are data from the first run. Solid circles are data from the second run corresponding to 41 h of beam on target. Curves are Monte Carlo simulations of the first run (dashed) and the second run (solid). The simulations were based on the calculations of Drake [12,66] for $Z=36$.

photon events from the high backgrounds encountered in the first run.

To see how the improved data analysis procedure eliminates the cascade-continuum coincidences, first note that these appear in both the horizontal and diagonal stripes in Fig. 12. When the horizontal stripes are projected onto the sum-energy axis, they give only a linear background under the peaks, so they do not contribute to the peak areas determined by the fits. The diagonal stripes produce peaks in the sum-energy spectra which move to the right as E_A increases (see Fig. 13). These ''moving peaks'' blend with the two-photon line in some spectra. In most cases, the peak-fitting procedure allowed us to extract the two-photon events from the blended peaks, but for some slices this was not possible to do reliably, so there are some gaps in the data presented in Fig. 14(a). Note that all of these occur above the midpoint of the distribution. This could have been anticipated from a study of Fig. 12, since the diagonal stripes intersect the two-photon stripe only in the region $E_A > E_0/2$.

In Fig. 14(b) we give the results of a similar analysis using sum-energy spectra cut on detector B. The data in Figs. 14(a) and 14(b) are not independent since they are just different analyses of the same events. Note that just as for the analysis based on cuts on E_A, all of the gaps in Fig. 14(b) (caused by unresolved blends) occur above the midpoint of the distribution. This suggested another way to group the data which avoids the problem of blended lines. We combined the data from Figs. 14(a) and 14(b) for the second run, adding the counts in each energy bin but keeping only the bins in the lower half of the distribution. The result is the ''folded spectrum'' displayed in Fig. 15(a). All the events are included in this figure, since, if E_A is greater than $E_0/2$, E_B must be less than $E_0/2$. Combining the data in this manner is justified since all of the theoretical distributions are symmetric about the midpoint. The folded spectrum provides the most stringent test of the theoretical calculations because combining the two halves of the distribution results in a reduction of the statistical errors. The solid line in the figure gives the Monte Carlo results using Drake's calculation of the shape for Kr ($Z=36$), while the dashed line is the result for helium ($Z=2$). Applying the χ^2 test to compare these curves with the experimental curve, we find $\chi_n^2 = 1.7$ for the $Z=36$ simulation and $\chi_n^2 = 5.2$ for the $Z=2$ simulation. This provides confirmation of the expected dependence of the He-like two-photon-continuum shape on Z.

The statistical error in the simulation is negligible compared to the errors due to the uncertainties in the input parameters. To determine the effect of these uncertainties, we began with an ''average curve'' found by running the simulation with the most probable values of the various input parameters. We then generated a series of curves with the simulation, changing one parameter at a time by adding and subtracting its standard deviation. All of the curves were binned in the same way, and renormalized to the average curve. In each bin the deviations from the average curve were computed and the root-mean-square deviation determined the error for that bin. This produced the error band for the simulation shown in Fig. 15(b), which also implicitly incorporates the statistical errors in the simulation as well. The special case of a possible ice layer was treated differently because of the asymmetry in that error (see Table II).
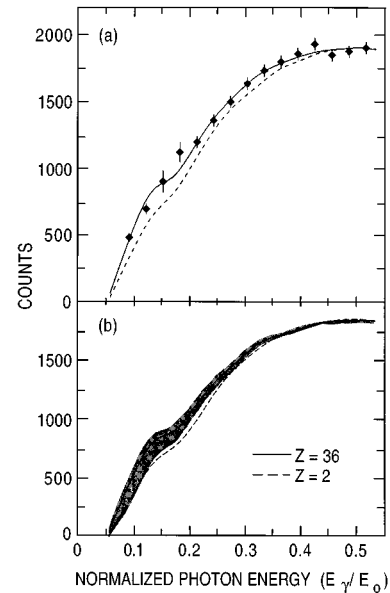

FIG. 15. (a) ''Folded'' continuum spectrum for the second run. These results were obtained by adding the data below the midpoints of the distributions in Figs. 14(a) and 14(b). The curves are the Monte Carlo results for $Z=2$ (dashed), and $Z=36$ (solid). (b) Simulation of the shape of the two-photon continuum radiation in He-like Kr ($Z=36$) for the first experimental run (solid line) and one standard deviation error limits on this simulation (shading). The dashed curve is a simulation based on the two-photon-continuum shape for helium $Z=2$. The curves in both (a) and (b) are normalized at the peak of the distribution.

The ice only contributes to the lower error limit and leads to an asymmetric band at low energies. In Fig. 15(b) we show the average curve and the error band for $Z=36$ together with a curve from a simulation based on the calculation for helium ($Z=2$). Figure 15(b) indicates that the uncertainties in the simulation are only slightly less than the difference between the calculated shapes for $Z=36$ and 2. Since the uncertainties in the data points of Fig. 15(a) are smaller than this, it is clear that the experiment is limited by the uncertainties in the input parameters to the simulation.

It would be difficult to reduce the uncertainties in the input parameters significantly, particularly with respect to the determination of the detector efficiencies. Factors such as the amount of ice buildup on the crystals can change periodically, so that, even if improved methods for determining the efficiencies were used, one could not be certain the characteristics of each detector would remain constant over an extended run. So a fundamental change in the experimental method may be needed for a more precise measurement.

One approach for an improved experiment would be to measure the shape of the two-photon continuum from both H- and He-like ions simultaneously. By periodically switching between these two species, changes in the experimental conditions could be averaged over. Assuming the H-like shape is known, such a measurement would give the continuum shape of the He-like two-photon decay, limited only by the statistical uncertainty. We are currently pursuing an experiment to compare the two-photon-continuum emission from the $2\,^2S_{1/2}$ level in H-like Ni with that from the $2\,^1S_0$ level in He-like Ni.

For testing the relativistic corrections, it is important to also make measurements in higher-Z ions where the relativistic corrections are larger. A measurement in a significantly heavier ion would also provide a confirmation of the Z dependence of the spectral shape, and elucidate two-photon decay in strong central fields. For these reasons an experiment is planned to measure the continuum radiation from He-like Pb at Gesellschaft für Schwerionenforschung (GSI) in Darmstadt.

Finally, it is hoped that the present experiment and the plans for future work in this area will stimulate further theoretical work, particularly a calculation of the relativistic corrections for heavy He-like ions.

[1] M. Göppert-Mayer, Ann. Phys. (Leipzig) **9**, 273 (1931).

[2] M. Göppert, Naturwissenschaften **17**, 932 (1929).

[3] B. E. J. Pagel, Nature **221**, 325 (1969).

[4] L. Spitzer, Jr. and J. L. Greenstein, Astrophys. J. **114**, 407 (1951).

[5] R. W. Dunford, H. G. Berry, S. Cheng, E. P. Kanter, C. Kurtz, B. J. Zabransky, A. E. Livingston, and L. J. Curtis, Phys. Rev. A **48**, 1929 (1993).

[6] R. Marrus, V. S. Vicente, P. Charles, J. P. Briand, F. Bosch, D. Liesen, and I. Varga, Phys. Rev. Lett. **56**, 1683 (1986).

[7] G. Breit and E. Teller, Astrophys. J. **91**, 215 (1940).

[8] J. Shapiro and G. Breit, Phys. Rev. **113**, 179 (1959).

[9] B. A. Zon and L. P. Rapoport, Pis'ma Zh. Éksp. Teor. Fis. **7**, 70 (1968) [JETP Lett. **7**, 52 (1968)].

[10] S. Klarsfeld, Phys. Lett. **30A**, 382 (1969).

[11] S. Klarsfeld, Lett. Nuovo Cimento **1**, 682 (1969).

[12] G. W. F. Drake, Phys. Rev. A **34**, 2871 (1986).

[13] C. K. Au, Phys. Rev. A **14**, 531 (1976).

[14] J. H. Tung, X. M. Ye, G. J. Salamo, and F. T. Chan, Phys. Rev. A **30**, 1175 (1984).

[15] V. Florescu, Phys. Rev. A **30**, 2441 (1984).

[16] V. Florescu, S. Pătrascu, and O. Stoican, Phys. Rev. A **36**, 2155 (1987).

[17] A. Dalgarno, Mon. Not. R. Astron. Soc. **131**, 311 (1966).

[18] A. Dalgarno and G. A. Victor, Proc. Phys. Soc. London **87**, 371 (1966).

[19] G. A. Victor and A. Dalgarno, Phys. Rev. Lett. **18**, 1105 (1967).

[20] G. A. Victor, Proc. Phys. Soc. London **91**, 825 (1967).

[21] V. Jacobs, Phys. Rev. A **4**, 939 (1971).

[22] G. W. F. Drake, G. A. Victor, and A. Dalgarno, Phys. Rev. **180**, 25 (1969).

[23] O. Bely, J. Phys. B **1**, 718 (1968).

[24] O. Bely and P. Faucher, Astron. Astrophys. **1**, 37 (1969).

[25] G. W. F. Drake and A. Dalgarno, Astrophys. J. **152**, L121 (1968).

[26] G. W. F. Drake, Nucl. Instrum. Methods Phys. Res. Sect. B **9**, 465 (1985).

[27] R. W. Dunford, Phys. Rev. A **54**, 3820 (1996).

[28] R. W. Schmieder, Phys. Rev. A **7**, 1458 (1973).

[29] R. Novick, in *Physics of the One and Two Electron Atoms*, edited by F. Bopp and H. Kleinpoppen (North-Holland, Amsterdam, 1969), p. 296.

[30] M. Lipeles, R. Novick, and N. Tolk, Phys. Rev. Lett. **15**, 690 (1965).

[31] C. J. Arthur, N. Tolk, and R. Novick, Astrophys. J. Lett. **157**, L181 (1969).

[32] R. W. Dunford, M. Hass, E. Bakke, H. G. Berry, C. J. Liu, M. L. A. Raphaelian, and L. J. Curtis, Phys. Rev. Lett. **62**, 2809 (1989).

[33] R. Marrus and R. W. Schmieder, Phys. Rev. A **5**, 1160 (1972).

[34] E. A. Hinds, J. E. Clendenin, and R. Novick, Phys. Rev. A **17**, 670 (1978).

[35] H. Gould and R. Marrus, Phys. Rev. A **28**, 2001 (1983).

[36] M. H. Prior, Phys. Rev. Lett. **29**, 611 (1972).

[37] C. L. Cocke, B. Curnutte, J. R. Macdonald, J. A. Bednar, and R. Marrus, Phys. Rev. A **9**, 2242 (1974).

[38] C. A. Kocher, J. E. Clendenin, and R. Novick, Phys. Rev. Lett. **29**, 615 (1972).

[39] S. Cheng, H. G. Berry, R. W. Dunford, D. S. Gemmell, E. P. Kanter, B. J. Zabransky, A. E. Livingston, L. J. Curtis, J. Bailey, and J. A. Nolen, Jr., Phys. Rev. A **47**, 903 (1993).

[40] H. Krüger and A. Oed, Phys. Lett. **54A**, 251 (1975).

[41] R. W. Dunford, H. G. Berry, D. A. Church, M. Hass, C. J. Liu, M. L. A. Raphaelian, B. J. Zabransky, L. J. Curtis, and A. E. Livingston, Phys. Rev. A **48**, 2729 (1993).

[42] A. Simionovici, B. B. Birkett, J. P. Briand, P. Charles, D. D. Dietrich, K. Finlayson, P. Indelicato, D. Liesen, and R. Marrus, Phys. Rev. A **48**, 1695 (1993).

[43] A. S. Pearl, Phys. Rev. Lett. **24**, 703 (1970).

[44] R. S. Van Dyck, Jr., C. E. Johnson, and H. A. Shugart, Phys. Rev. A **4**, 1327 (1971).

[45] M. H. Prior and H. A. Shugart, Phys. Rev. Lett. **27**, 902 (1971).

[46] I. Freund, Phys. Rev. A **7**, 1849 (1973).

[47] Y.-J. Wu and J.-M. Li, J. Phys. B **21**, 1509 (1988).

[48] Y. B. Bannett and I. Freund, Phys. Rev. A **30**, 299 (1984).

[49] J. Eichler, Phys. Rev. A **9**, 1762 (1974).

[50] T. Åberg, in *Atomic Inner-Shell Processes*, edited by B. Crasemann (Academic, New York, 1975), p. 353.

[51] X.-M. Tong, J.-M. Li, L. Kissel, and R. H. Pratt, Phys. Rev. A **42**, 1442 (1990).

[52] X. Mu and B. Crasemann, Phys. Rev. A **38**, 4585 (1988).

[53] D.-S. Guo, Phys. Rev. A **36**, 4267 (1987).

[54] Y. Bannett and I. Freund, Phys. Rev. Lett. **49**, 539 (1982).

[55] K. Ilakovac, J. Tudorić-Ghemo, B. Bušić, and V. Horvat, Phys. Rev. Lett. **56**, 2469 (1986).

[56] K. Ilakovac, J. Tudorić-Ghemo, and S. Kaučić, Phys. Rev. A **44**, 7392 (1991).

[57] K. Ilakovac, V. Horvat, Z. Krečak, G. Jerbić-Zorc, N. Ilakovac, and T. Bokulić, Phys. Rev. A **46**, 132 (1992).

[58] J. Schirmer, D. Habs, R. Kroth, N. Kwong, D. Schwalm, M. Zirnbauer, and C. Broude, Phys. Rev. Lett. **53**, 1897 (1984).

[59] J. Kramp, D. Habs, R. Kroth, M. Music, J. Schirmer, D. Schwalm, and C. Broude, Nucl. Phys. A **474**, 412 (1987).

[60] M. E. Rose and G. E. Uhlenbeck, Phys. Rev. **48**, 211 (1935).

[61] M. E. Rose, Phys. Rev. **76**, 678 (1949).

[62] S. P. Goldman and G. W. F. Drake, Phys. Rev. A **24**, 183 (1981).

[63] W. R. Johnson, Phys. Rev. Lett. **29**, 1123 (1972).

[64] F. A. Parpia and W. R. Johnson, Phys. Rev. A **26**, 1142 (1982).

[65] S. P. Goldman, Phys. Rev. A **40**, 1185 (1989).

[66] G. W. F. Drake (unpublished).

[67] R. C. Elton, L. J. Palumbo, and H. R. Griem, Phys. Rev. Lett. **20**, 783 (1968).

[68] D. O'Connell, K. J. Kollath, A. J. Duncan, and H. Kleinpoppen, J. Phys. B **8**, L214 (1975).

[69] R. W. Schmieder and R. Marrus, Phys. Rev. Lett. **25**, 1692 (1970).

[70] P. H. Mokler, S. Reusch, A. Warczak, Z. Stachura, T. Kambara, A. Müller, R. Schuch, and M. Schulz, Phys. Rev. Lett. **65**, 3108 (1990).

[71] T. Stöhlker, C. Kozhuharov, A. E. Livingston, P. H. Mokler, J. Ullrich, and B. Fricke, Z. Phys. D **21**, S233 (1991).

[72] P. H. Mokler, in *Recombination of Atomic Ions*, Vol. 299 of *NATO Advanced Study Institute Series B: Physics*, edited by

W. G. Graham, W. Fritsch, Y. Hahn, and J. A. Tanis (Plenum, New York, 1992), p. 259.

[73] Th. Stöhlker (unpublished).

[74] R. Ali, I. Ahmad, H. G. Berry, R. W. Dunford, D. S. Gemmell, E. P. Kanter, P. H. Mokler, A. E. Livingston, S. Cheng, and L. J. Curtis, Nucl. Instrum. Methods Phys. Res. Sect. B **98**, 69 (1995).

[75] J. S. Hansen, J. C. McGeorge, D. Nix, W. D. Schmidt-Ott, I. Unus, and R. W. Fink, Nucl. Instrum. Methods **106**, 365 (1973).

[76] Z. B. Alfassi and R. Nothman, Nucl. Instrum. Methods **143**, 57 (1977).

[77] D. D. Cohen, Nucl. Instrum Methods **178**, 481 (1980).

[78] D. D. Cohen, Nucl. Instrum. Methods **193**, 15 (1982).

[79] D. D. Cohen, Nucl. Instrum. Methods Phys. Res. Sect. A **267**, 492 (1988).

[80] J. L. Campbell and P. L. McGhee, Nucl. Instrum. Methods Phys. Res. Sect. A **248**, 393 (1986).

[81] K. Shima, S. Nagai, T. Mikumo, and S. Yasumi, Nucl. Instrum. Methods **217**, 515 (1983). We also used information from a subsequent ATLAS run in which the continuum radiation from two-photon decay of Ar^{17+} was studied in the vicinity of the silicon K edge.

[82] E. Storm and H. I. Israel, Nucl. Data Tables A **7**, 565 (1970).

[83] Source code for the simulation program is available at ftp://anlphy.phy.anl.gov/mc2p.

[84] R. Pardo, B. E. Clifft, P. Denhartog, D. Kovar, W. Kutschera, and K. E. Rehm, Nucl. Instrum. Methods Phys. Res. Sect. A **270**, 226 (1988).

[85] S. Cheng, R. W. Dunford, C. J. Liu, B. J. Zabransky, A. E. Livingston, and L. J. Curtis, Phys. Rev. A **49**, 2347 (1994).